The Astrophysical Journal, 606:1057–1069, 2004 May 10

THE *r*-PROCESS IN SUPERNOVAE: IMPACT OF NEW MICROSCOPIC MASS FORMULAE

Shinya Wanajo,[1] Stephane Goriely,[2] Mathieu Samyn,[2] and Naoki Itoh[1]
Received 2003 November 10; accepted 2004 January 23

ABSTRACT

The astrophysical origin of *r*-process nuclei is a long-standing mystery. Although some astrophysical scenarios show some promise, many uncertainties involved in both the astrophysical conditions and in the nuclear properties far from the β-stability have inhibited us from understanding the nature of the *r*-process. The purpose of the present paper is to examine the effects of the newly derived microscopic Hartree-Fock-Bogoliubov (HFB) mass formulae on *r*-process nucleosynthesis and analyze to what extent a solar-like *r*-abundance distribution can be obtained. The *r*-process calculations with the HFB-2 mass formula are performed, adopting the parameterized model of the prompt explosion from a collapsing O-Ne-Mg core for the physical conditions, and compared with the results obtained with the HFB-7 and droplet-type mass formulae. Because of its weak shell effect at the neutron magic numbers in the neutron-rich region, the microscopic mass formulae (HFB-2 and HFB-7) give rise to a spread of the abundance distribution in the vicinity of the *r*-process peaks ($A = 130$ and 195). While this effect resolves the large underproduction at $A \approx 115$ and 140 obtained with droplet-type mass formulae, large deviations compared to the solar pattern are found near the third *r*-process peak. It is shown that a solar-like *r*-process pattern can be obtained if the dynamical timescales of the outgoing mass trajectories are increased by a factor of about 2–3, or if the β-decay rates are systematically increased by the same factor.

Subject headings: nuclear reactions, nucleosynthesis, abundances — stars: abundances — supernovae: general

1. INTRODUCTION

The origin of the rapid–neutron-capture (*r*-process) nuclei is still a mystery. One of the underlying difficulties is that the astrophysical site (and consequently the astrophysical conditions) in which the *r*-process takes place has not been identified. Although some scenarios such as "neutrino-driven winds" from nascent neutron stars (Woosley et al. 1994; Takahashi, Witti, & Janka 1994; Qian & Woosley 1996; Cardall & Fuller 1997; Otsuki et al. 2000; Wanajo et al. 2001; Thompson, Burrows, & Meyer 2001), "prompt supernova explosions" from small iron cores (Sumiyoshi et al. 2001) or from O-Ne-Mg cores (Wanajo et al. 2003), and "neutron star mergers" (Freiburghaus, Rosswog, & Thielemann 1999b) show some promise, each of them faces severe problems and cannot at the present time be called on to explain the production and galactic enrichment of the *r*-process nuclei observed in nature.

Another underlying difficulty is the uncertainties in the theoretical predictions of nuclear data far from the β-stability, for which essentially no experimental data exist. In particular, mass predictions for neutron-rich nuclei play a key role since they affect all the nuclear quantities of relevance in the *r*-process, namely the neutron-capture, photodisintegration, and β-decay rates, as well as the fission probabilities. Although most of the recent mass formulae show fits to experimental masses of similar quality (characterized by an rms error of about 0.7 MeV), the mass extrapolations far from the valley of β-stability can differ from each other quite significantly (for a recent review, see Lunney, Pearson, & Thibault 2003). Recently, Hartree-Fock mass formulae with fully microscopic approaches have been constructed (Goriely, Tondeur, & Pearson 2001; Samyn et al. 2002; Goriely et al. 2002, 2004; Samyn, Goriely, & Pearson 2003). The latest Hartree-Fock-Bogoliubov formulae, labeled HFB-2 through HFB-7 (Goriely et al. 2002, 2004; Samyn et al. 2003), are among the most accurate mass formulae, predicting the 2135 measured masses with an rms error around 0.670 MeV for nuclei with $N, Z \geq 8$, i.e., with the same accuracy or even better than the one obtained with droplet-like mass formulae (Hilf, von Groote, & Takahashi 1976; Möller et al. 1995). A brief comparison of these mass models is given in § 2.

The purpose of this study is to examine the effects of the newly derived microscopic mass formula on *r*-process nucleosynthesis and analyze to what extent a solar-like distribution can be obtained. Most of previous works devoted to the study of nuclear mass formulae and their impact on *r*-process nucleosynthesis were based on *site-independent* approaches, the so-called canonical model assuming a constant temperature and neutron number density during the neutron-capture phase (Goriely & Arnould 1996, 2001; Cowan et al. 1999; Goriely & Clerbaux 1999; Schatz et al. 2002). This approach is understandable since the astrophysical *r*-process site has not been unambiguously identified. Another approach consists of considering promising sites and modifying some of the relevant characteristics to force a successful *r*-process. In this case, the free parameter space is usually reduced and an easier analysis can be performed. In addition, some works based on such *site-specific* approaches have demonstrated that the abundance distributions are sensitive to the astrophysical conditions adopted, particularly during the "freezeout" phase (Surman et al. 1997; Freiburghaus et al. 1999a; Surman & Engel 2001; Wanajo et al. 2002).

We adopt here for the physical conditions the semirealistic astrophysical model of the "prompt supernova explosion" from the collapsing O-Ne-Mg core by Wanajo et al. (2003) (§ 3). The *r*-process nucleosynthesis with the HFB-2 mass formula in each outgoing mass trajectory is then calculated

[1] Department of Physics, Sophia University, 7-1 Kioi-cho, Chiyoda-ku, Tokyo 102-8554, Japan; wanajo@sophia.ac.jp, n_itoh@sophia.ac.jp.
[2] Institut d'Astronomie et d'Astrophysique, C.P. 226, Université Libre de Bruxelles, B-1050 Brussels, Belgium; sgoriely@astro.ulb.ac.be.

with a nuclear reaction network code. The mass-averaged yields over the mass shells relevant for the *r*-process are compared with the *r*-process abundance patterns in the solar system and in an extremely metal-poor star (CS 22892-052), as well as with those obtained with other mass formulae, more specifically the HFB-7 mass prediction and the extensively used droplet formulae of Hilf et al. (1976) and Möller et al. (1995) (§ 4). Uncertainties stemming from the astrophysical conditions and extranuclear ingredients are discussed in § 5. A summary follows in § 6.

2. MICROSCOPIC MASS MODELS

Among the ground-state properties, the atomic mass is obviously the most fundamental quantity and influences the *r*-process abundance predictions mainly through the (n, γ)-(γ, n) competition taking place in the neutron-rich region. The calculation of the reaction rates also requires the knowledge of other ground-state properties, such as the deformation, density distribution, single-particle level scheme, pairing force, and shell correction energies. Recently, impressive progress has been made experimentally. This situation results largely from recent measurements with Penning-trap or Schottky spectrometers that have enlarged the region of known masses, particularly toward the neutron-deficient side of the valley of nuclear stability (for a recent review, see Lunney et al. 2003). The new Atomic Mass Evaluation (G. Audi & A. H. Wapstra 2001, private communication) contains 2214 measured masses, i.e., 250 more than the 1995 one (Audi & Wapstra 1995). A more accurate mass determination is also available now for about 132 nuclides originally included in the 1995 compilation. Out of the 382 new experimental masses, 337 are located in the proton-rich region of the nuclear chart and only 45 in the neutron-rich region. As far as nuclei directly involved in the *r*-process are concerned, almost no experimental mass data exist, and theory must fill the gap.

Attempts to estimate nuclear masses go back to the liquid-drop Weizsäcker mass formula. Improvements to this original model have been made little by little, leading to the development of macroscopic-microscopic mass formulae, such as the droplet model (DM; e.g., Hilf et al. 1976) and the finite-range droplet model (FRDM) of Möller et al. (1995). In this framework, the macroscopic contribution to the masses and the microscopic corrections of a phenomenological nature are treated independently, both parts being connected solely through a parameter fitted to experimental masses. Despite the great empirical success of these formulae (e.g., FRDM fits the 2135 $Z \geq 8$ experimental masses [G. Audi & A. H. Wapstra 2001, private communication] with an rms error of 0.676 MeV), they suffer from major shortcomings, such as the incoherence of the link between the macroscopic part and the microscopic correction, the instability of the mass prediction to different parameter sets, or the instability of the shell corrections. As a consequence, their reliability when extrapolating far from experimentally known masses is severely limited. Although these models have been extensively used for astrophysical applications (Woosley et al. 1994; Takahashi et al. 1994; Sumiyoshi et al. 2001; Wanajo et al. 2001, 2002, 2003), there is an obvious need to develop a mass model that is more closely connected to the basic nuclear interaction properties.

A new major progress has been achieved recently within the Hartree-Fock method (Goriely et al. 2001, 2002, 2004; Samyn et al. 2002, 2003). It is now demonstrated that this microscopic approach, making use of a Skyrme force fitted to essentially all the mass data, is not only feasible but can

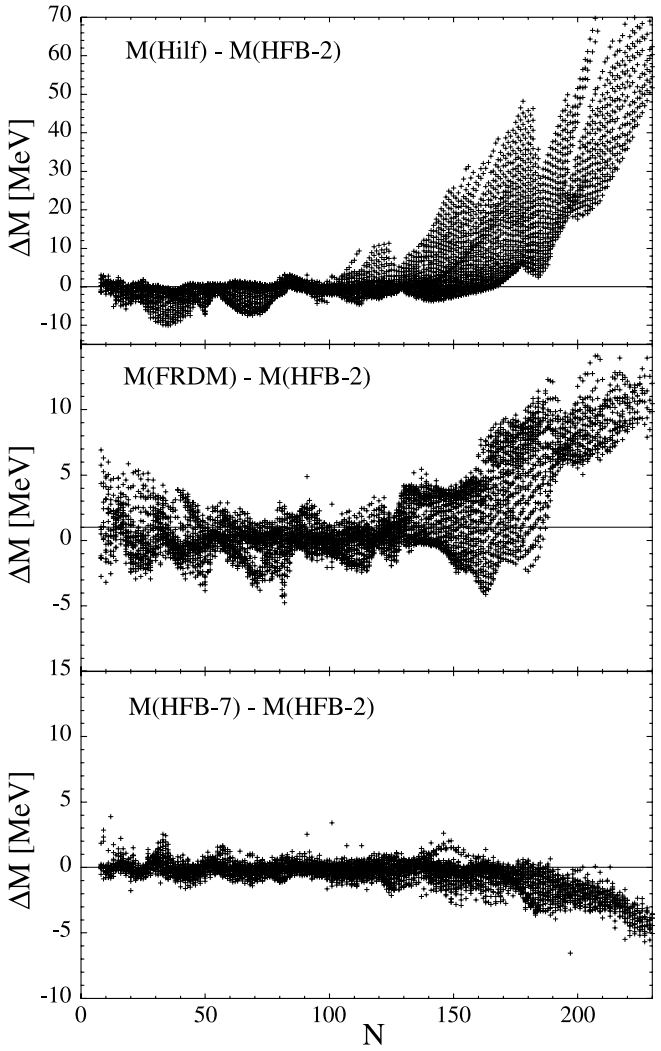

FIG. 1.—Mass differences between HFB-2 and the DM of Hilf et al. (1976; *top*), HFB-2 and the FRDM of Möller et al. (1995; *middle*), and HFB-2 and HFB-7 (*bottom*) as a function of the neutron number N for all nuclei with $Z, N \geq 8$ lying between the proton and the neutron drip lines up to $Z = 110$.

successfully compete with the most accurate droplet-like formulae available nowadays in the reproduction of measured masses. This holds true not only when the pairing force is described in the Bardeen-Cooper-Schrieffer approximation but also when the Bogoliubov method is adopted (HFB model), which has the advantage of ensuring the self-consistency of the treatment of the nuclear single-particle and pairing properties. These large-scale HFB calculations are based on the conventional 10-parameter Skyrme force, along with a four-parameter δ-function pairing force. The Skyrme and pairing parameters are derived from a fit to the full data set of 2135 measured masses of nuclei with $Z, N \geq 8$, leading to an rms error of the order of 0.674 MeV for the HFB-2 mass table.

Despite the success of the HFB-2 mass formula, a series of studies of possible modifications to the basic force model and to the method of calculation was initiated all within the HFB framework in order to test the reliability of the mass extrapolations (Samyn et al. 2003; Goriely et al. 2004). For this reason, a set of five additional new mass tables, referred to as HFB-3 through HFB-7, were designed to analyze the sensitivity of the mass fit and extrapolations to the prescription

used for the center-of-mass correction, the density-dependence of the pairing interaction, and the amplitude of the effective nucleon mass. The new mass fits are of the same quality as the HFB-2 mass predictions. In addition, it is found that globally the extrapolations out to the neutron drip line of all these different HFB mass formulae are essentially equivalent. Figure 1 (*bottom*) compares the HFB-2 and HFB-7 masses for all nuclei with $8 \leq Z \leq 110$ lying between the proton and neutron drip lines. Although HFB-2 and HFB-7 are obtained with significantly different Skyrme forces (in particular, HFB-2 is characterized by a density-independent pairing force and an effective isoscalar mass $M_s^* = 1.04$, while HFB-7 has an density-dependent pairing force and $M_s^* = 0.8$), deviations smaller than about 2 MeV are obtained for nuclei with $Z \leq 82$.

In contrast, more discrepancies are seen between HFB and droplet-type masses (Fig. 1), especially for superheavy nuclei. For lighter species, the mass differences remain below some 5–10 MeV, although significantly different shell and deformation effects are predicted. Most particularly, the HFB mass formulae show a weaker neutron-shell closure close to the neutron drip line with respect to droplet-like models such as FRDM (for a more detailed discussion, see Goriely et al. 2002). Future improved microscopic predictions, particularly in mean-field but also in shell-model approaches, as well as future experiments, will hopefully shed light on the behavior of the $N = 82$ and 126 neutron-shell closures at large isospins, in a way similar to that for the $N = 20$, 28, and 50 magic numbers (Lunney et al. 2003). These major differences in the nuclear structure properties may affect the nucleosynthesis predictions, as shown in § 4.

3. SUPERNOVA MODEL AND THE *r*-PROCESS

Recent comprehensive spectroscopic studies of extremely metal-poor stars in the Galactic halo (Hill et al. 2002; Cowan et al. 2002; Sneden et al. 2003), as well as chemical evolution studies (Ishimaru & Wanajo 1999; Ishimaru et al. 2004; Argast et al. 2004), suggest that the *r*-process is a primary nucleosynthesis process and that the astrophysical site could be associated with core-collapse supernovae. In fact, most of the recent studies on *r*-process nucleosynthesis have been based on the "neutrino-driven wind" scenario, in which the free nucleons accelerated by the intense neutrino flux near the neutrino sphere of a core-collapse supernova join together and form heavier nuclei (Woosley et al. 1994; Qian & Woosley 1996; Cardall & Fuller 1997; Otsuki et al. 2000; Wanajo et al. 2001; Thompson et al. 2001).

In the present study, we use the parameterized model of the prompt supernova explosion from an 8–10 $M_\odot$ progenitor star (with a 1.38 $M_\odot$ O-Ne-Mg core) by Wanajo et al. (2003). This model leads to *r*-abundance distributions that have been shown to be relatively similar to the solar distribution, at least if an artificial enhancement of the shock-heating energy is assumed. In addition, this scenario does not suffer from the problematic overproduction of $A \approx 90$ nuclei seen in the neutrino-driven wind model (Woosley et al. 1994; Wanajo et al. 2001). Finally, the physical conditions in hydrodynamic (i.e., prompt) explosions may not be significantly affected by highly uncertain neutrino heating (or cooling) processes (Hillebrandt, Nomoto, & Wolff 1984), as they are in the neutrino wind model. The site modeling is consequently easier, and the final abundance predictions are less sensitive to the neutrino physics. All these reasons justify the present study and the comparison of the nucleosynthesis results with the solar *r*-abundance distribution. It is obvious, however, that a similar study based on the neutrino-driven wind scenario is needed since the prompt-explosion scenario also faces severe problems that need to be resolved (Wanajo et al. 2003). In particular, it should be recalled here that in consistent realistic prompt-explosion models, only a weak explosion is obtained, and no *r*-processing. An artificial enhancement of the shock energy is needed to drive an energetic explosion and provide the necessary conditions for a successful *r*-process.

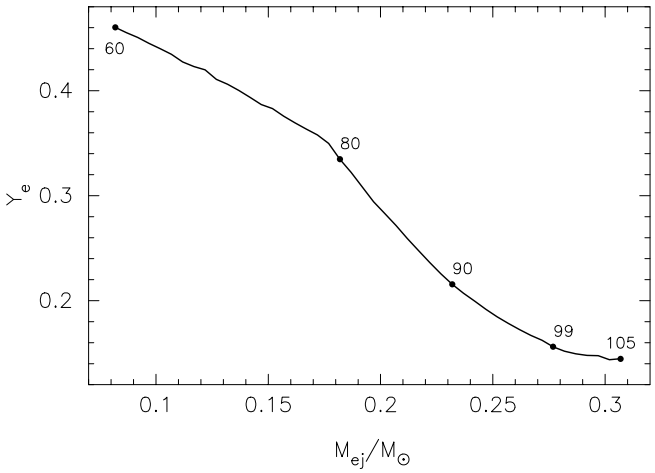

FIG. 2.—Distribution of the initial electron mole fraction in the ejected matter adopted in this study. The surface of the O-Ne-Mg core is at mass coordinate zero. Selected mass elements are denoted by zone numbers.

Wanajo et al. (2003) performed core-collapse simulations with a one-dimensional, Newtonian hydrodynamic code. The highly neutronized ejecta (Y_{e0}, initial electron mole fraction $\approx$0.14–0.20) in the (artificial) energetic explosion (model Q6) is subject to a strong production of *r*-process nuclei. In this study, we use the mass trajectories of the ejected material from $M_{\rm ej} = 0.08\ M_\odot$ (zone number 60, $Y_{e0} = 0.45$) to $0.31\ M_\odot$ (zone number 105, $Y_{e0} = 0.14$) in mass coordinate (the surface of the O-Ne-Mg core is at mass coordinate zero), as shown in Figure 2. This mass range was shown by Wanajo et al. (2003) to give a solar-like *r*-abundance distribution, assuming that part of the ejected material with low Y_e (layers 106–132 of Wanajo et al. 2003) was artificially assumed to be reaccreted onto the compact object and consequently to not contribute to galactic enrichment. The temperature and density histories of some mass elements are presented in Figure 3.

Adopting model Q6 in Wanajo et al. (2003) for the physical conditions, the *r*-process abundances are obtained by solving an extensive nuclear reaction network code. The network consists of $\sim$4400 species, all the way from single neutrons and protons up to the fermium ($Z = 100$) isotopes (Fig. 4). We include all relevant reactions, i.e., (n,γ), (p,γ), (α,γ), (p,n), (α,n), and (α,p), and the inverse of each. All reaction rates are calculated within the statistical model of Hauser-Feshbach, making use of experimental masses (G. Audi & A. H. Wapstra 2001, private communication) whenever available, or the HFB-2 mass predictions (Goriely et al. 2002) otherwise. The photodisintegration rates are deduced from the reverse (n,γ) rates, applying the reciprocity theorem with the nuclear masses considered. The β-decay and β-delayed neutron emission rates are taken from the gross theory (GT2) of Tachibana, Yamada, & Yoshida (1990), obtained with the ETFSI (extended Thomas-Fermi plus Strutinsky integral; Aboussir et al. 1995) Q_β predictions. Other nuclear inputs are the same as in Wanajo et al. (2003).

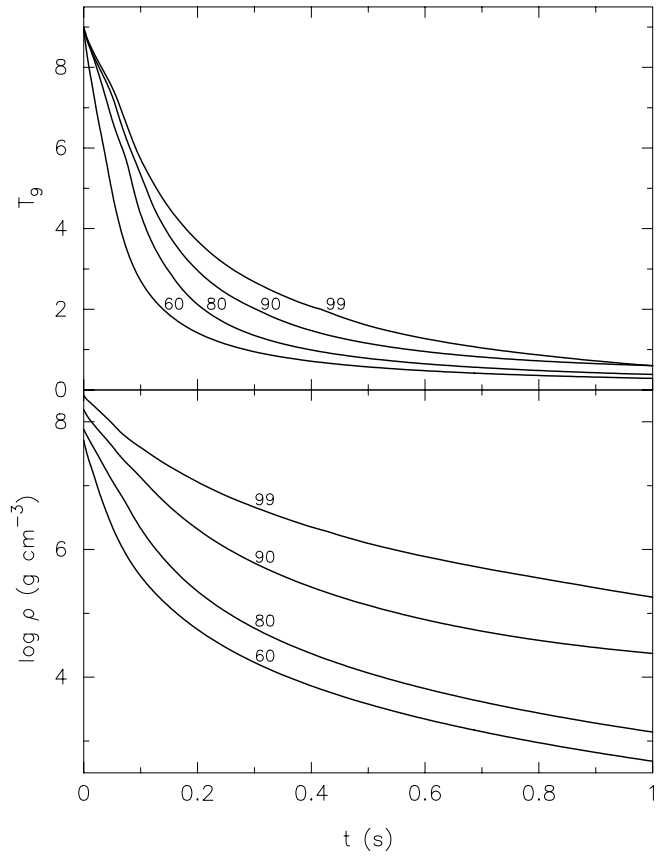

FIG. 3.—Temperature (*top*; $T_9 \equiv 10^9$ K) and density (*bottom*) histories for selected mass elements, which are denoted by zone numbers. Time is set to zero at $T_9 = 9$.

A word of caution is required concerning some inconsistencies in the nuclear input considered here, most particularly concerning the use of ETFSI masses to estimate β-decay rates within the GT2 model. As mentioned in § 2, nuclear masses influence the *r*-abundance distribution mainly through the (n,γ)-(γ,n) competition taking place in the neutron-rich region. Thanks to the balance theorem, such a competition remains relatively independent of the model adopted to estimate the neutron-capture and photodisintegration rates. In contrast, the sensitivity of the absolute value of the reaction and β-decay rates on nuclear masses can depend significantly on the model considered. For example, within the statistical GT2 model, the β-decay rates scale as the fifth power of the Q_β value, while in the continuum QRPA model (e.g., Borzov & Goriely 2003), the rates depend on the possible spin-isospin excitation within the Q_β window but are not directly affected by the nuclear mass as such. Ultimately, for each mass model, a consistent estimate of the reaction and β-decay rates based on the corresponding mass model predictions for masses, but also deformation, single-particle properties, etc., should be performed. In order to simplify here the discussion on the impact of masses, but also to avoid the complicated model dependence in the estimate of the reaction and β-decay rates, we restrict ourselves to considering in all cases only one set of β-decay rates, namely the GT2 rates with ETFSI masses.

The calculation in each mass trajectory is started at $T_9 = 9$ (where $T_9 \equiv T/10^9$ K). The initial composition is taken to be that of the nuclear statistical equilibrium with the matter density ρ at $T_9 = 9$ and consists mostly of free nucleons and α-particles. The calculation is terminated 10 s after the start in each mass trajectory. Snapshots of the *r*-process calculation in mass-trajectory 99 (1.11 $M_\odot$ mass coordinate and $Y_{e0} = 0.16$) are shown in Figure 4. The abundances (mole fractions) are color coded, while the isotopes included in the reaction network are shown by dots, with the stable and metastable isotopes shown by larger dots. Contours of constant two-neutron–separation energies divided by two ($S_{2n}/2$) from 1 to 8 MeV are superposed. The abundance curve as a function of the mass number is also shown on the upper left of each panel.

The top panel of Figure 4 shows the time slice when the neutron-to-seed ratio Y_n/Y_h decreases to $\sim$1, where Y_n is the abundance of free neutrons and

$$Y_h \equiv \sum_{Z>2,A} Y(Z,A) \qquad (1)$$

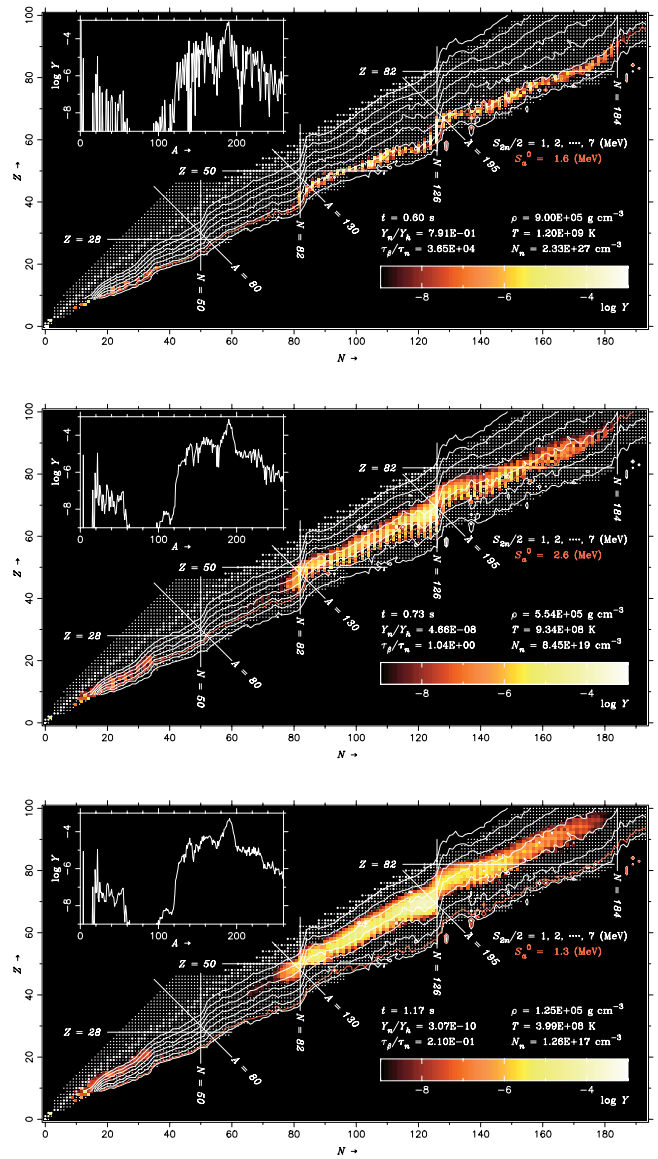

FIG. 4.—Abundance distributions at neutron exhaustion ($Y_n/Y_h \sim 1$; *top*), freezeout ($\tau_\beta/\tau_n \sim 1$; *middle*), and later times (*bottom*) for trajectory 99 (see text). The abundances are color coded in the nuclide chart. The abundance curve as a function of mass number is shown on the upper left of each panel. The nuclei included in the reaction network are denoted by dots, with the stable and long-lived isotopes represented by large dots. Iso-$S_{2n}/2$ (=1, 2, . . . , 7 MeV) and S_a^0 curves are also superposed.

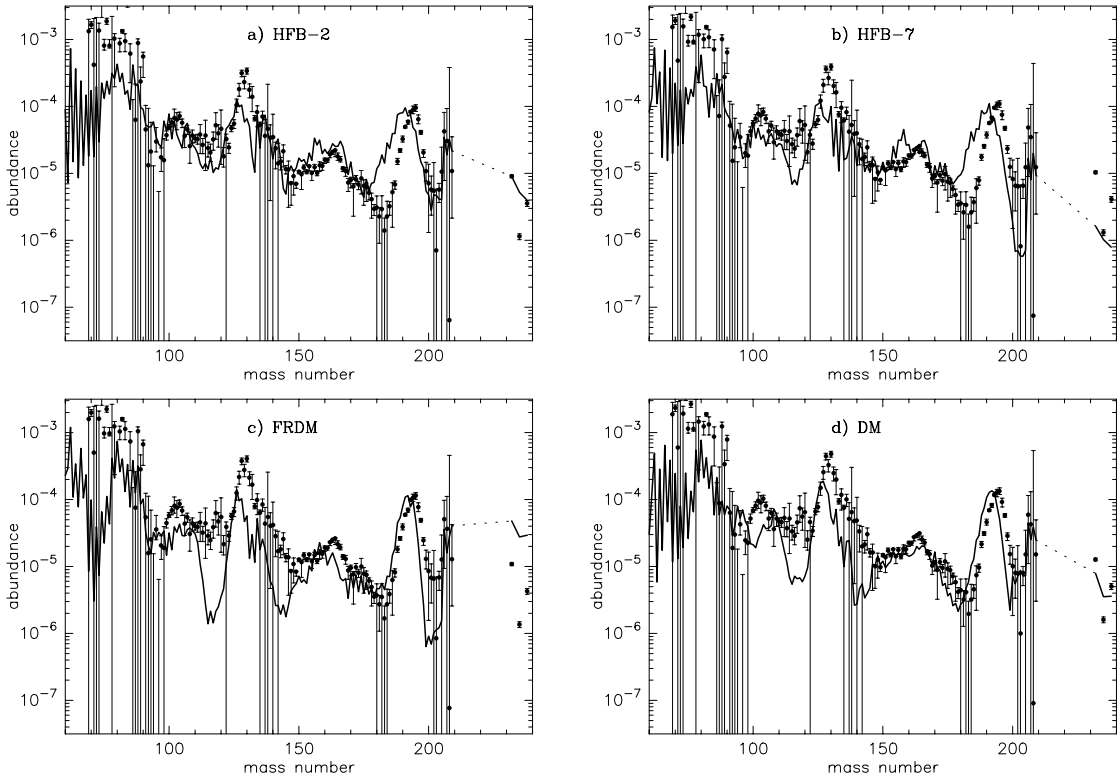

FIG. 5.—Final mass-averaged *r*-process abundances (*line*) as a function of mass number obtained with various mass formulae: (*a*) HFB-2, (*b*) HFB-7, (*c*) FRDM, and (*d*) DM. These are compared with the solar *r*-process abundances (*points*) from Goriely (1999), which are scaled to match the height of the third *r*-process peak.

is that of nuclei heavier than helium. At this time, the *r*-process flow closely follows an iso-S_{2n} curve given by $S_{2n}/2 = S_a^0 \approx 1.6$ MeV (*red line*), where

$$S_a^0\,(\mathrm{MeV}) \equiv \left(34.075 - \log N_n + \frac{3}{2}\log T_9\right)\frac{T_9}{5.04}; \quad (2)$$

N_n is the number density of free neutrons in units of cm^{-3}. The condition $Y_n/Y_h = 1$ is referred to as "neutron exhaustion."

For the adopted (n,γ) rates, a quasi-equilibrium between neutron capture and photodisintegration continues until τ_β/τ_n decreases to $\sim$1, as can be seen in the middle panel of Figure 4, where

$$\tau_\beta \equiv \left[\frac{1}{Y_h}\sum_{Z>2,A}\lambda_\beta(Z,A)\,Y(Z,A)\right]^{-1}, \quad (3)$$

$$\tau_n \equiv \left[\frac{\rho Y_n}{Y_h}\sum_{Z>2,A}\lambda_n(Z,A)\,Y(Z,A)\right]^{-1} \quad (4)$$

are the averaged β-decay and neutron-capture lifetimes and $\lambda_\beta(Z,A)$, $\lambda_n(Z,A)$ are the β-decay and neutron-capture rates of the nucleus (Z,A), respectively. At this time, the abundance distribution is still near the $S_a^0 \approx 2.6$ MeV line. We refer hereafter to the condition $\tau_\beta/\tau_n = 1$ as "freezeout" and to the epoch between neutron exhaustion and freezeout as the "freezeout phase." This freezeout phase is of particular relevance in determining the final abundance pattern, as discussed in § 4. After freezeout, the global abundance pattern is not significantly affected anymore, although it can still be somewhat smoothed out by photodisintegration and β-delayed neutron emission, as can be seen in the bottom panel of Figure 4 ($\tau_\beta/\tau_n \approx 0.2$).

4. IMPACT OF MASS PREDICTIONS ON THE *r*-PROCESS

The final *r*-process yields are mass-averaged over all mass trajectories between mass coordinates of 1.08 and 1.30 $M_\odot$. In Figure 5*a*, the mass-averaged abundances (*line*) are compared with the solar *r*-process abundance pattern (*points*; Goriely 1999), which is scaled to match the height of the third *r*-process peak. For comparison, identical calculations were performed by replacing our standard HFB-2 masses by the HFB-7 (Goriely et al. 2004; Fig. 5*b*), FRDM (Möller et al. 1995; Fig. 5*c*), and DM (Hilf et al. 1976; Fig. 5*d*) predictions.

Roughly speaking, an overall agreement between calculated and solar abundance curves can be seen in Figures 5*a*–5*d* for nuclei with $A = 100$–200. Discrepancies common to all cases are, however, observed, in particular the deficiencies for nuclei in the vicinity of the first *r*-process peak ($A = 80$), the shifts with respect to the solar curve of the second and third *r*-process peaks ($A = 130$ and 195) to lower mass numbers ($\sim$3 units in mass number), and the ratio of second to third peak height, which is significantly smaller than observed in the solar distribution. We do not discuss further the deficiencies near $A = 80$, since theoretically the results are highly dependent on the adopted mass cut of the ejecta (see § 3 and Wanajo et al. 2003 for more details), and observationally there has been an increasing amount of evidences that the light ($A < 130$) *r*-process nuclei have a different origin than the heavy ($A > 130$) ones (e.g., Hill et al. 2002; Sneden et al. 2003). For the shifts of the peak locations, as well as the second-to-third peak ratio, it is conceivable that this deficiency does not come from the mass model but rather from

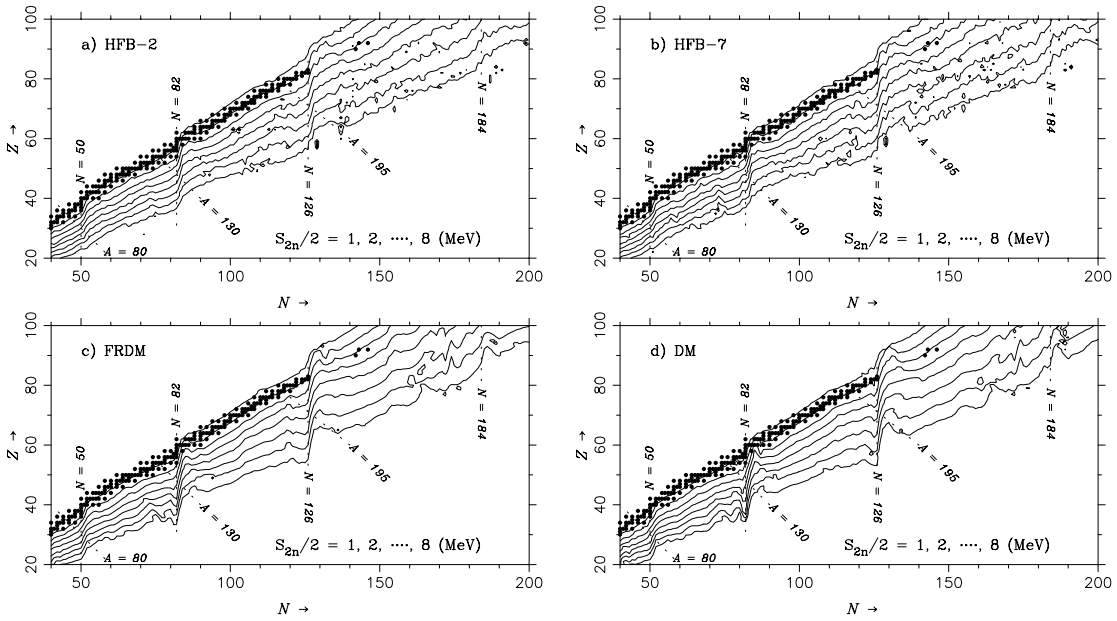

FIG. 6.—Contours of the $S_{2n}/2$ values (=1, 2, . . . , 8 MeV) for various mass formulae: (*a*) HFB-2, (*b*) HFB-7, (*c*) FRDM, and (*d*) DM. The stable and long-lived isotopes are also represented by dots.

inadequate astrophysical or nuclear description, since it is observed for all mass formulae. This point is further discussed in § 5.

A few significant differences in the abundance patterns can, however, be observed near the second and third peaks when use is made of the Hartree-Fock models (HFB-2 and HFB-7) on one side and the droplet models on the other side. First, the underproduction of nuclei at $A \approx 115$ and 140 is more pronounced with the FRDM (Fig. 5*c*) and DM (Fig. 5*d*) masses than with the HFB-2 (Fig. 5*a*) or HFB-7 (Fig. 5*b*) masses. Second, the abundances near $A = 130$ in the HFB cases are spread out, in contrast to what is observed in the solar *r*-abundances. Third, the abundance curves near the third peak with the HFB masses are widened, and the valley at $A = 183$ as observed in the solar *r*-distribution is significantly shifted to lower mass numbers.

These differences reflect the model properties of the iso-$S_{2n}/2$ curves shown in Figure 6, along which the *r*-process proceeds (see also Fig. 4). Major local differences between the HFB (Figs. 6*a* and 6*b*) and the droplet masses (Figs. 6*c* and 6*d*) are found near the neutron magic numbers $N = 82$ and 126. The Hartree-Fock masses show weaker shell closures, i.e., smoother iso-$S_{2n}/2$ curves, at $N = 82$ and 126. This reduced shell effect (which actually is not totally quenched at the neutron drip line, in contrast with other predictions, e.g., Pearson, Nayak, & Goriely 1996) is responsible for spreading the second and third abundance peaks. In contrast, the large droplet shell effect is clearly seen at $N = 82$ and 126 by the steep $S_{2n}/2$ character even close to the neutron drip line and gives rise to sharp abundance peaks.

Figure 7 illustrates the formation process of the second and third peaks with the HFB-2 masses in more details. The left panels show the snapshots of the abundance distributions for trajectory 90 (1.15 $M_\odot$ mass coordinate and $Y_{e0} = 0.23$) and the right panels show those for trajectory 99 (1.11 $M_\odot$ mass coordinate and $Y_{e0} = 0.16$) at neutron exhaustion (*top panels*), freezeout (*middle panels*), and later times (*bottom panels*). Trajectory 90 (Fig. 7, *left panels*) gives a major contribution to the second-peak formation. The abundances are widely distributed already at neutron exhaustion (*top left*), owing to the weaker shell gaps at $N = 82$, especially for low $S_{2n}/2$. This results in a split of the second abundance peak, as seen in Figure 5*a*. The shift of the abundance distribution to the heavier mass number during the freezeout phase is small, although the abundance curve is significantly smoothed by photodisintegration (and slightly by β-delayed emission). The reason is that the freezeout takes place at a low S_a^0 value ($\approx$2.9 MeV; Fig. 7, *middle left*).

The formation process of the third peak in trajectory 99 can be seen in the right panels of Figure 7. The $N = 126$ shell effect in the neutron-rich region is not reduced like the $N = 82$ one, although it still remains weaker than in the droplet approach. The splitting of the peak abundances is not observed, but the abundance curve is significantly broaden by photodisintegrations during the freezeout phase. The freezeout takes place when S_a^0 is still low (2.6 MeV), and for this reason the peak position at $A = 190$ is not shifted during the freezeout phase.

Some of the deficiencies observed in the *r*-abundance distribution obtained with HFB masses are seen to be cured when considering droplet masses (Fig. 5). In particular, the DM masses characterized by isospin-independent $N = 82$ and $N = 126$ shell effects give rise to an abundance curve that is seen to be globally in better agreement with the solar pattern than are the HFB curves. It would be tempting to judge the quality of the nuclear mass predictions on the basis of such a comparison. However, it must be recalled here that such *r*-process calculations in prompt-explosion scenarios (as in any other site studied so far) remain strongly affected by other input uncertainties in the astrophysical modeling, as well as by extranuclear ingredients. More specifically, the total mass finally ejected (i.e., not reaccreted onto the proto–neutron star) remains unknown and strongly dependent on the astrophysical modeling of the explosion. The same holds for the dynamical timescale of the outgoing material. Finally, major difficulties still exist in predicting reliably the β-decay

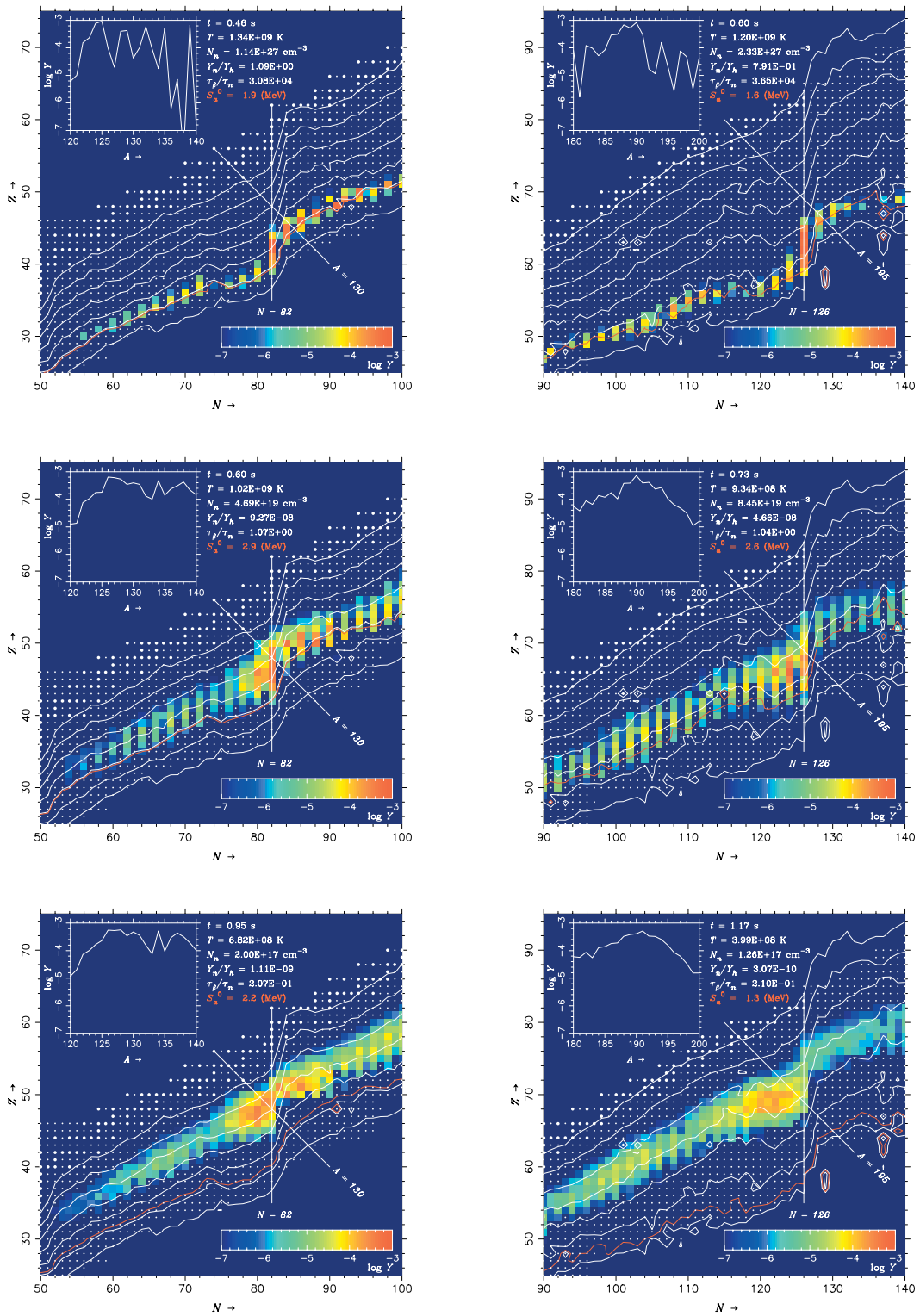

FIG. 7.—Same as Fig. 4, but near the second peak ($A \approx 130$) with trajectory 90 (*left panels*) and the third peak ($A \approx 195$) with trajectory 99 (*right panels*)

half-lives of exotic neutron-rich nuclei. These uncertainties are studied in § 5, where it is shown that a modification of either the physical conditions of the explosion or the β-decay rates can influence drastically the agreement with the solar *r*-distribution.

Finally, it could also be argued that the outcome of prompt-explosion nucleosynthesis in one specific star might not need to match the solar *r*-process pattern. Recent spectroscopic studies show that the elemental abundance patterns between the second and third peaks of *r*-process–enhanced ultra–metal-poor stars in the Galactic halo are in excellent agreement with the solar *r*-process abundances. In particular, the agreement extends to the third-peak elements Os, Ir, and Pt for HD 115444, HD 126238 (Sneden et al. 1998), BD +17°3248 (Cowan et al. 2002), CS 22892-052 (Sneden et al. 2003; Fig. 8), and CS 31082-001 (Hill et al. 2002). These observations led

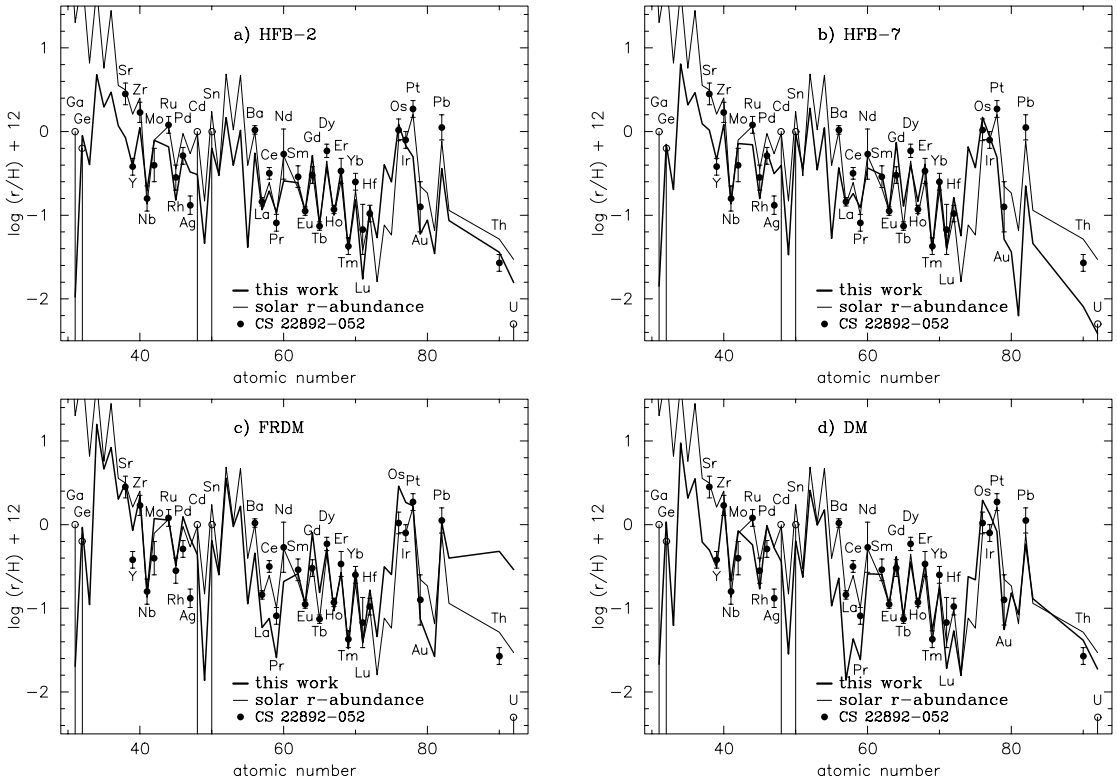

FIG. 8.—Comparison of the mass-averaged yields (*thick line*) obtained with the HFB-2 masses, scaled at Eu ($Z = 63$), with the abundance pattern of CS 22892-052 (*filled circles with observational error bars*), as a function of atomic number. For Ga, Ge, Cd, Sn, and U, the observed upper limits are shown by the open circles. The scaled solar *r*-process pattern is shown by the thin line.

these authors to the conclusion that there is only one single *r*-process site that contributes to the production of heavy ($A > 130$) *r*-process nuclei and that the corresponding distribution is similar to the solar *r*-process pattern (Sneden et al. 1996). Instead of comparing the predicted abundances with the solar content, we can therefore use such observations and estimate the extent to which the disagreements seen in Figure 5 and discussed above are also reflected in the comparison with the observed elemental distribution. The comparison is shown in Figure 8 for the most studied extremely metal-poor star CS 22892-052 (Sneden et al. 2003). Even in this case, it is difficult to discriminate between the predictions obtained with the four different mass formulae considered here. This is quite normal since the observed distribution is reduced to some 30 elements (in comparison with some 130 nuclei in the solar material). And above all, the observed pattern could well be explained by nuclear property invariance in the $56 \leq Z \leq 76$ region rather than by specific astrophysical conditions, as discussed in Goriely & Arnould (1997). It is therefore more informative to compare the *r*-abundance prediction with the solar pattern, keeping in mind that there is no stringent observational constraint that the final distribution should be strictly solar. Nevertheless, future abundance determinations of as many extremely metal-poor stars as possible will be of particular importance in shedding light on nucleosynthesis yields from only one or a few supernova events.

5. UNCERTAINTIES IN THE *r*-PROCESS CALCULATIONS

In this section we examine possible astrophysical and nuclear modifications leading to a better agreement of the HFB-2 abundance curve with the solar *r*-process pattern. Regarding the prompt supernova explosions considered here, we do not expect the entropy per baryon of the shocked material to be very different from the one deduced from the simulation ($\sim$10 in units of the Boltzmann constant), since many previous simulations resulted in similar values (Hillebrandt et al. 1984; Sumiyoshi et al. 2001). However, the dynamical timescale of the outgoing matter (without changing the entropy) can significantly differ from model to model. For example, the dynamical timescales of the mass trajectories responsible for the *r*-process in Sumiyoshi et al. (2001) are typically a few times shorter than those applied in this study (Wanajo et al. 2003), because of their different treatments of electron capture. It is also conceivable that other effects, such as convection, asymmetric explosion, or reverse shock from the outer envelope, cause an acceleration or a deceleration of the outgoing material.

In order to test the impact of a change in the dynamical timescales, we simply modify the density and temperature profiles of each trajectory, so that $\rho'(t) = \rho(t/f_t)$ and $T'(t) = T(t/f_t)$, i.e., the dynamical timescale is multiplied by a factor of f_t. Figures 9 and 10 show the abundance curves for $f_t =$ 0.2, 0.5 (fast), 1 (standard), 2, 3, and 5 (slow) obtained with mass trajectories 90 and 99, which are responsible for the formation of the second and third peaks, respectively. The abundance curves near the second (Fig. 9) and third (Fig. 10) peaks are seen to agree fairly well with to the solar *r*-process pattern when the timescale is multiplied by a factor of 2–3 (Figs. 9*d*–9*e* and 10*d*–10*e*) and to disagree for the fast trajectories (Figs. 9*a*–9*b* and 10*a*–10*b*).

This temporal effect is due to the significant abundance evolution during the freezeout phase for the slowly outgoing

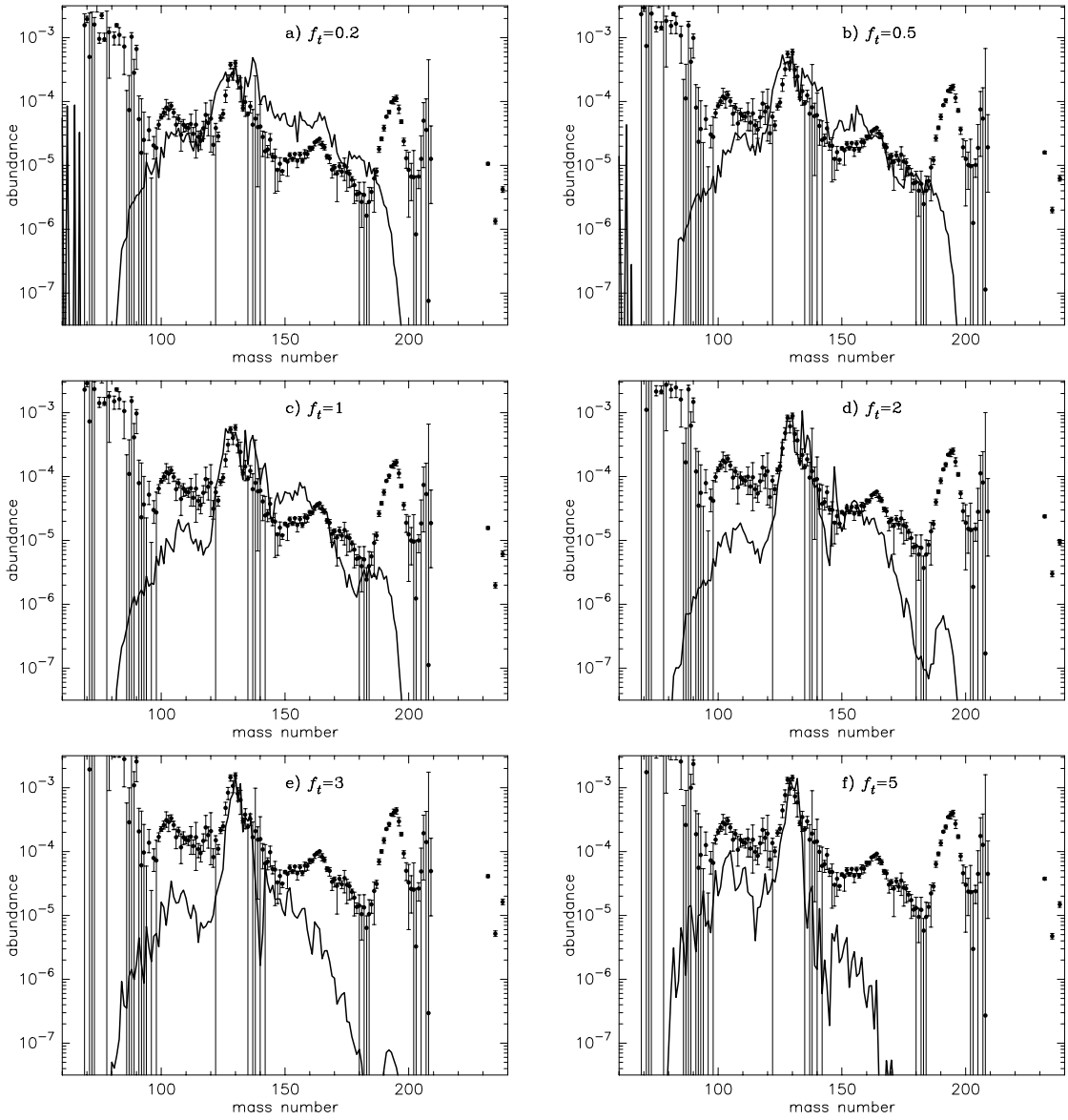

FIG. 9.—Final abundances as a function of mass number from *r*-process calculations for trajectory 90 with f_t = (*a*) 0.2, (*b*) 0.5, (*c*) 1, (*d*) 2, (*e*) 3, and (*f*) 5 (see text). These are compared with the solar *r*-process abundances (*points*) from Goriely (1999), which are scaled to match the height of the second *r*-process peak.

material, as shown in Figure 11 (same as Fig. 7, but for $f_t = 3$). At the neutron exhaustion, the abundances are dispersed near the second (*top left panel*) and third (*top right panel*) peaks, owing to the weak shell gaps at $N = 82$ and 126 for low $S_{2n}/2$ ($\approx$2–3 MeV), as in the standard case (Fig. 7). The freezeout takes place (*middle panels*), however, at much higher S_a^0 values (4.2 and 3.7 MeV for trajectories 90 and 99, respectively) than those in the standard case (2.9 and 2.6 MeV; Fig. 7). The reason is that the temperatures at the freezeout are higher ($T_9 = 1.4$ and 1.2 for trajectories 90 and 99, respectively) owing to the slow expansion with $f_t = 3$ than those in the standard case ($T_9 =$ 1.0 and 0.93). As a result, the abundance peaks shift to $A = 130$ (trajectory 90) and 194 (trajectory 99), i.e., mostly at the same position as those in the solar *r*-distribution. Concomitantly, the width of the abundance curve near the second and third peaks is reduced significantly because of the larger shell gaps at $S_a^0 \approx 4$ MeV than that at $S_a^0 \lesssim 3$ MeV and becomes similar to the one observed in the solar pattern (Figs. 9*e* and 10*e*).

If all the nuclear inputs are correct and the *r*-process indeed originates in the collapse of the O-Ne-Mg core, the implication is that the expansion of the outgoing material must be significantly slower than obtained by Wanajo et al. (2003). A possible explanation could be found in the deceleration of the ejecta by the reverse shock from the outer envelope if the hydrogen and helium layers survive the mass loss until the onset of the core collapse. This effect is absent from the simulation of Wanajo et al. (2003) with a bare O-Ne-Mg white dwarf. This reverse shock effect would also reduce the total overproduction of *r*-processed material per event in the prompt-explosion scenario (see Wanajo et al. 2003). It is interesting to note that such a significant deceleration of the outgoing material takes place in the neutrino-powered explosion because of the stalled shock wall once launched by a core bounce (Woosley et al. 1994). More detailed numerical simulations of the collapsing O-Ne-Mg core including the outer envelope are needed to quantify this effect.

The final mass-averaged abundance curve corresponding to mass trajectories slowed by a factor of 3 ($f_t = 3$) is shown

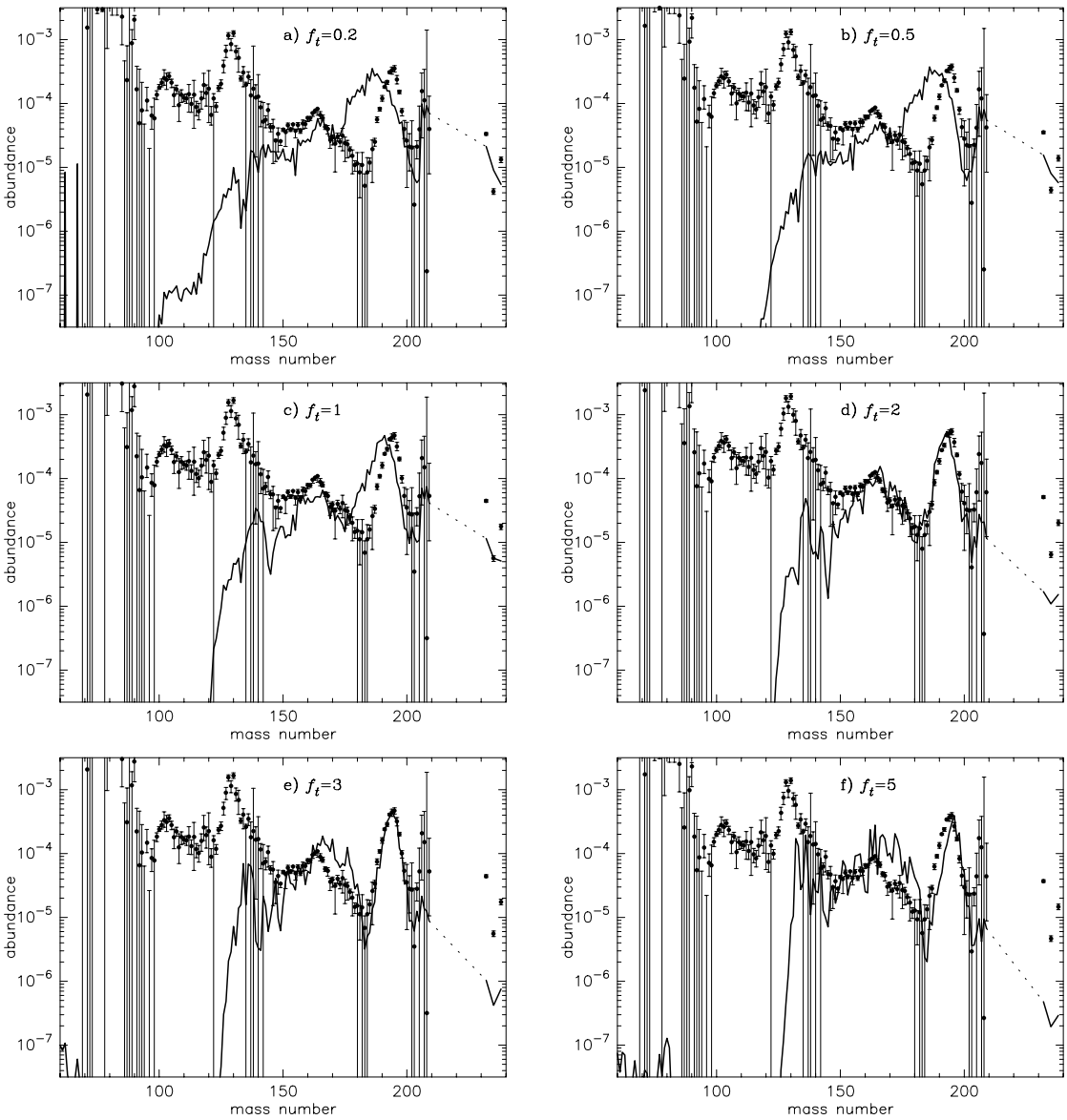

FIG. 10.—Same as Fig. 9, but for trajectory 99. The solar *r*-process abundances (*points*) from Goriely (1999) are scaled to match the height of the third *r*-process peak.

with the scaled solar *r*-process abundances in Figure 12*a*. We find a good agreement between the calculated and solar *r*-process patterns, in particular near the second and third peaks. The steep valley at $A \approx 183$ observed in the solar *r*-process abundances is also well reproduced. However, an underproduction at $A \approx 115$ and 140 appear.

As far as nuclear uncertainties are concerned, β-decay rates, neutron-capture rates, and fission probabilities also play a key role (neutrino reactions are not important in the prompt explosion; see Wanajo et al. 2003). A change in their uncertain prediction can affect the nucleosynthesis predictions. In the present scenario, fission does not play an important role, however, since it affects only a small fraction of the total *r*-processed matter (Wanajo et al. 2003). The prediction of neutron-capture rates, especially for exotic neutron-rich nuclei, remains difficult, especially in the prediction of the direct-capture contribution, the γ-ray strength, and the neutron-nucleus optical model potential for exotic neutron-rich nuclei, as required in the statistical reaction model of Hauser-Feshbach (for more details, see Goriely 1997, 2003). Much work remains to be done to estimate the neutron capture rates reliably. For this reason, their impact on *r*-process nucleosynthesis is postponed to a future study.

Recent microscopic calculations of the β-decay rate within the energy density functional plus continuum QRPA formalism show that the first forbidden transitions might have been underestimated in the past and can increase the β-decay rate by a factor of about 2 along the neutron-rich $N = 82$ isotone and by a factor of about 3–10 along the neutron-rich $N = 126$ isotone, compared with the calculation based exclusively on the allowed transitions (Borzov 2003). Detailed microscopic estimates of the β-decay rates (including forbidden transitions) for all nuclei of relevance in *r*-process calculations, as well as future experiments with radioactive ion beams, are eagerly awaited for improving this fundamental input in the description of *r*-process nucleosynthesis.

To estimate the influence of β-decays, we show in Figure 12*b* the mass-averaged *r*-process yields obtained by multiplying all

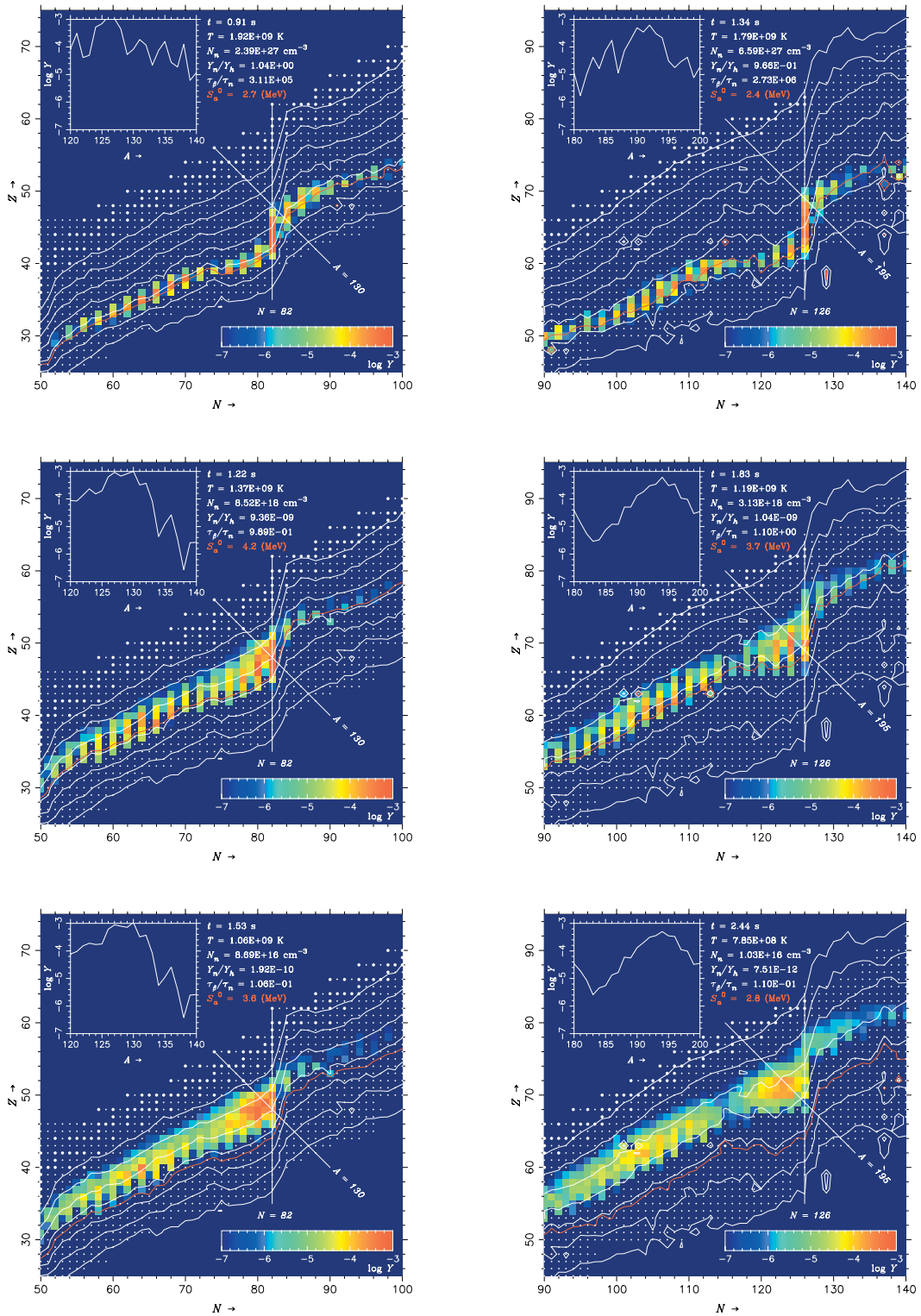

FIG. 11.—Same as Fig. 7, but for $f_t = 3$ (see text)

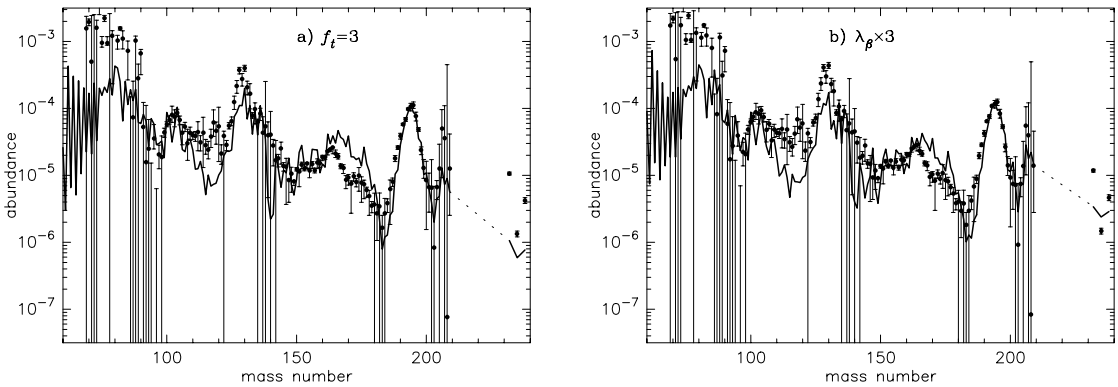

FIG. 12.—Same as Fig. 5, but for (*a*) slow trajectories ($f_t = 3$) and (*b*) fast β-decay rates (a factor of 3; see text)

the β-decay rates by a factor of 3 (i.e., reducing τ_β by a factor of 3). Interestingly, no significant differences are seen between Figures 12*a* and 12*b*. For β-decay rates faster by a factor of 3, the freezeout (corresponding to $\tau_\beta = \tau_n$) takes place at higher temperatures and thus at higher S_a^0 values, which has globally the same effect as slowing down the outgoing material by the same factor. This test calculation shows the crucial role played by β-decay rates when considering nonparameterized density and temperature profiles, i.e., thermodynamic conditions fixed by (semi)realistic models.

6. SUMMARY

We have examined *r*-process nucleosynthesis with a state-of-the-art microscopic mass formula, HFB-2 (Goriely et al. 2002), to see its effects on the theoretical *r*-process abundance prediction. The yields of *r*-process species were calculated with a nuclear reaction network code (∼4400 isotopes), adopting favorable physical conditions in the prompt-explosion model of a collapsing O-Ne-Mg core by Wanajo et al. (2003). This model led to production of the solar-like *r*-abundance pattern in the previous study (Wanajo et al. 2003). However, an artificial enhancement of the shock-heating energy was needed to obtain requisite physical conditions for successful *r*-processing.

Because of its weak shell effect at the neutron magic numbers in the neutron-rich region, the microscopic mass formulae (HFB-2 and HFB-7) give rise to a spread of the abundance distribution in the vicinity of the *r*-process peaks ($A = 130$ and 195). While this effect resolves the large underproduction at $A \approx 115$ and 140 obtained with droplet-type mass formulae, large deviations compared to the solar pattern are found near the third *r*-process peak. When use is made of droplet mass predictions, sharp *r*-process peaks are systematically found, owing to their strong shell effect for neutron magic numbers even in the neutron-rich region. However, because of the numerous uncertainties still affecting the astrophysical models, as well as the prediction of extranuclear ingredients, it would be highly premature to judge the quality of the mass formula on the basis of such a comparison.

We found that abundance peaks similar to the one observed in the solar system could be recovered if the dynamical timescales of the mass trajectories were increased by a factor of ∼2–3 (without any change in the entropy) or if the β-decay half-lives were systematically decreased by the same factor. These changes might be conceivable when considering the current uncertainties in the astrophysical as well as in the nuclear β-decay models. Much effort in astrophysical and nuclear modeling is still needed to improve the difficult description of *r*-process nucleosynthesis.

This work was supported by Grants-in-Aid for Scientific Research (13640245, 13740129) from the Ministry of Education, Culture, Sports, Science, and Technology of Japan. M. S. and S. G. are FNRS Research Fellow and Associate, respectively.

REFERENCES

Aboussir, Y., Pearson, J. M., Dutta, A. K., & Tondeur, F. 1995, At. Data Nucl. Data Tables, 61, 127
Argast, D., Samland, M., Thielemann, F.-K., & Qian, Y.-Z. 2004, A&A, 416, 997
Audi, G., & Wapstra, A. H. 1995, Nucl. Phys. A, 595, 409
Borzov, I. N. 2003, Phys. Rev. C, 67, 025802
Borzov, I. N., & Goriely, S. 2003, Phys. Part. Nuclei, 34, 1
Cardall, C. Y., & Fuller, G. M. 1997, ApJ, 486, L111
Cowan, J. J., Pfeiffer, B., Kratz, K.-L., Thielemann, F.-K., Sneden, C., Burles, S., Tytler, D., & Beers, T. C. 1999, ApJ, 521, 194
Cowan, J. J., et al. 2002, ApJ, 572, 861
Freiburghaus, C., Rembges, J.-F., Rauscher, T., Kolbe, E., Thielemann, F.-K., Kratz, K.-L., Pfeiffer, B., & Cowan, J. J. 1999a, ApJ, 516, 381
Freiburghaus, C., Rosswog, S., & Thielemann, F.-K. 1999b, ApJ, 525, L121
Goriely, S. 1997, A&A, 325, 414
———. 1999, A&A, 342, 881
———. 2003, Nucl. Phys. A, 718, 287
Goriely, S., & Arnould, M. 1996, A&A, 312, 327
———. 1997, A&A, 322, L29
———. 2001, A&A, 379, 1113
Goriely, S., & Clerbaux, B. 1999, A&A, 346, 798
Goriely, S., Samyn, M., Bender, M., & Pearson, J. M. 2004, Phys. Rev. C, in press
Goriely, S., Samyn, M., Heenen, P.-H., Pearson, J. M., & Tondeur, F. 2002, Phys. Rev. C, 66, 24326
Goriely, S., Tondeur, F., & Pearson, J. M. 2001, At. Data Nucl. Data Tables, 77, 311
Hilf, E. R., von Groote, H., & Takahashi, K. 1976, in Proc. Third International Conference on Nuclei Far from Stability (Geneva: CERN), 142
Hill, V., et al. 2002, A&A, 387, 560
Hillebrandt, W., Nomoto, K., & Wolff, G. 1984, A&A, 133, 175
Ishimaru, Y., & Wanajo, S. 1999, ApJ, 511, L33
Ishimaru, Y., Wanajo, S., Aoki, W., & Ryan, S. G. 2004, ApJ, 600, L47
Lunney, D., Pearson, J. M., & Thibault, C. 2003, Rev. Mod. Phys., 75, 1021
Möller, P., Nix, J. R., Myers, W. D., & Swiatecki, W. J. 1995, At. Data Nucl. Data Tables, 59, 185
Otsuki, K., Tagoshi, H., Kajino, T., & Wanajo, S. 2000, ApJ, 533, 424
Pearson, J. M., Nayak, R. C., & Goriely, S. 1996, Phys. Lett. B, 387, 455
Qian, Y.-Z., & Woosley, S. E. 1996, ApJ, 471, 331

Samyn, M., Goriely, S., Heenen, P.-H., Pearson, J. M., & Tondeur, F. 2002, Nucl. Phys. A, 700, 142
Samyn, M., Goriely, S., & Pearson, J. M. 2003, Nucl. Phys. A, 725, 69
Schatz, H., Toenjes, R., Kratz, K.-L., Pfeiffer, B., Beers, T. C., Cowan, J. J., & Hill, V. 2002, ApJ, 579, 626
Sneden, C., Cowan, J. J., Debra, L. B., & Truran, J. W. 1998, ApJ, 496, 235
Sneden, C., McWilliam, A., Preston, G. W., Cowan, J. J., Burris, D. L., & Armosky, B. J. 1996, ApJ, 467, 819
Sneden, C., et al. 2003, ApJ, 591, 936
Sumiyoshi, K., Terasawa, M., Mathews, G. J., Kajino, T., Yamada, S., & Suzuki, H. 2001, ApJ, 562, 880
Surman, R., & Engel, J. 2001, Phys. Rev. C, 64, 35801
Surman, R., Engel, J., Bennett, J. R., & Meyer, B. S. 1997, Phys. Rev. Lett., 79, 1809
Tachibana, T., Yamada, M., & Yoshida, Y. 1990, Prog. Theor. Phys., 84, 641
Takahashi, K., Witti, J., & Janka, H.-Th. 1994, A&A, 286, 857
Thompson, T. A., Burrows, A., & Meyer, B. S. 2001, ApJ, 562, 887
Wanajo, S., Itoh, N., Ishimaru, Y., Nozawa, S., & Beers, T. C. 2002, ApJ, 577, 853
Wanajo, S., Kajino, T., Mathews, G. J., & Otsuki, K. 2001, ApJ, 554, 578
Wanajo, S., Tamamura, M., Itoh, N., Nomoto, K., Ishimaru, Y., Beers, T. C., & Nozawa, S. 2003, ApJ, 593, 968
Woosley, S. E., Wilson, J. R., Mathews, G. J., Hoffman, R. D., & Meyer, B. S. 1994, ApJ, 433, 229